

CoMFA and CoMSIA investigations of dopamine D₃ receptor ligands leading to the prediction, synthesis, and evaluation of rigidized FAUC 365 analogues

Ismail Salama, Karin Schlotter, Wolfgang Utz, Harald Hübner,
Peter Gmeiner and Frank Boeckler*

*Department of Medicinal Chemistry, Emil Fischer Center, Friedrich Alexander University,
Schuhstraße 19, D-91052 Erlangen, Germany*

Received 23 March 2006; revised 5 May 2006; accepted 15 May 2006
Available online 5 June 2006

Abstract—Taking advantage of our in-house experimental data on dopamine D₃ receptor modulators, we have successfully established highly significant CoMFA and CoMSIA models ($q_{cv}^2 = 0.82/0.76$). These models were carefully investigated to assure their stability and predictivity ($r_{pred}^2 = 0.65/0.61$) and subsequently applied to guide experimental investigations on the synthesis and receptor binding of three conformationally restricted D₃ ligands. Besides the high D₃ affinity, the test compound **45**, incorporating a *trans*-1,4-cyclohexylene partial structure, exhibited improved (~3200-fold) selectivity over the D₄ subtype.
© 2006 Elsevier Ltd. All rights reserved.

1. Introduction

In more than 15 years of research since the discovery of the D₃ receptor by Sokoloff and coworkers,¹ enormous progress has been made toward improving our understanding of its physiological function and pharmacological impact. As the D₃ receptor is preferentially located in brain regions which have an impact on emotional and cognitive functions, it is able to affect behavioral properties, such as locomotor activity, reinforcement, and reward. Thus, various pharmacological studies have investigated it as an interesting therapeutic target for the treatment of schizophrenia,^{2,3} Parkinson's disease,⁴ drug-induced dyskinesia,⁵ and drug abuse (in particular cocaine addiction).^{3,6} Moreover, D₃ might be involved in the cortical development during gestation when it obviously regulates neuronal migration and differentiation.⁷ Parallel to gaining a more detailed insight into D₃ receptor pharmacology and into the evaluation of respective treatment opportunities, the available D₃ ligands have undergone a 'structural evolution'.⁸ Mostly driven by rational drug discovery, small, dopamine-

related agonists have evolved into structurally diverse agents with high affinity, selectivity over the closely related biogenic amine receptors, and a broad range of intrinsic activities. In recent years, 4-phenylpiperazine has obtained a predominant position as a building block in D₃-selective ligands. Although this 'privileged structure' has already been a frequently used scaffold for other biogenic amine receptors including the dopamine D₄ receptor subtype,^{9–12} tuning of the substitution pattern of the phenyl moiety and, in particular, tuning of the spacer length and type between a (hetero)aromatic moiety and the piperazine has yielded series of ligands with highly interesting D₃ receptor binding and activation profiles.^{8,13} Among these, for example, BP 897 (**27**) has been intensely investigated for its putative use in the treatment of cocaine addiction^{6,14} and L-DOPA induced dyskinesia in patients with Parkinson's disease.⁵ We have recently demonstrated that the pyrazolo[1,5-*a*]pyridine analogue FAUC 329 (**3**) exerts neuroprotective effects in the MPTP (1-methyl-4-phenyl-1,2,3,6-tetrahydropyridine) mouse model of Parkinson's disease.¹⁵ Its closely related bioisostere FAUC 365 has been described as the most selective D₃ antagonist, yet.¹⁶

Taking advantage of our in-house data on D₃ ligands,^{16–18} we herein present a ligand-based 3D-QSAR approach (Chart 1) in order to improve and refine our understanding of the molecular requirements for optimized D₃

Keywords: 3D-QSAR; Dopamine D₃ Receptor; Phenylpiperazine; CoMFA/CoMSIA model.

* Corresponding author. Tel.: +49 9131 8524115; fax: +49 9131 8522585; e-mail: boeckler@pharmazie.uni-erlangen.de

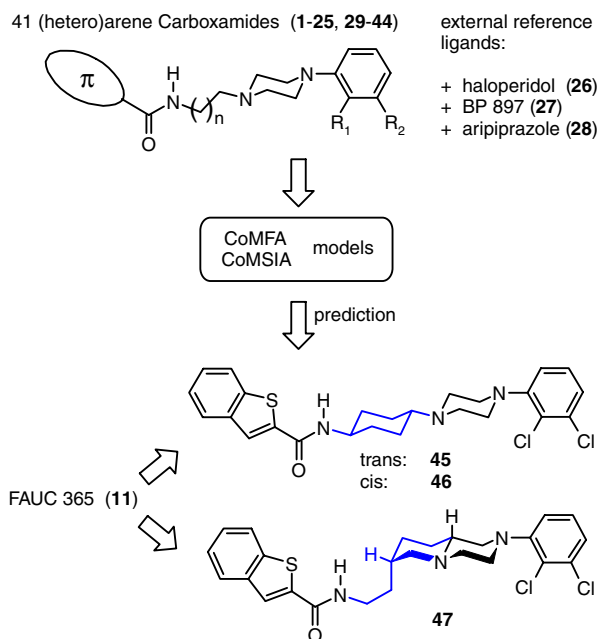


Chart 1.

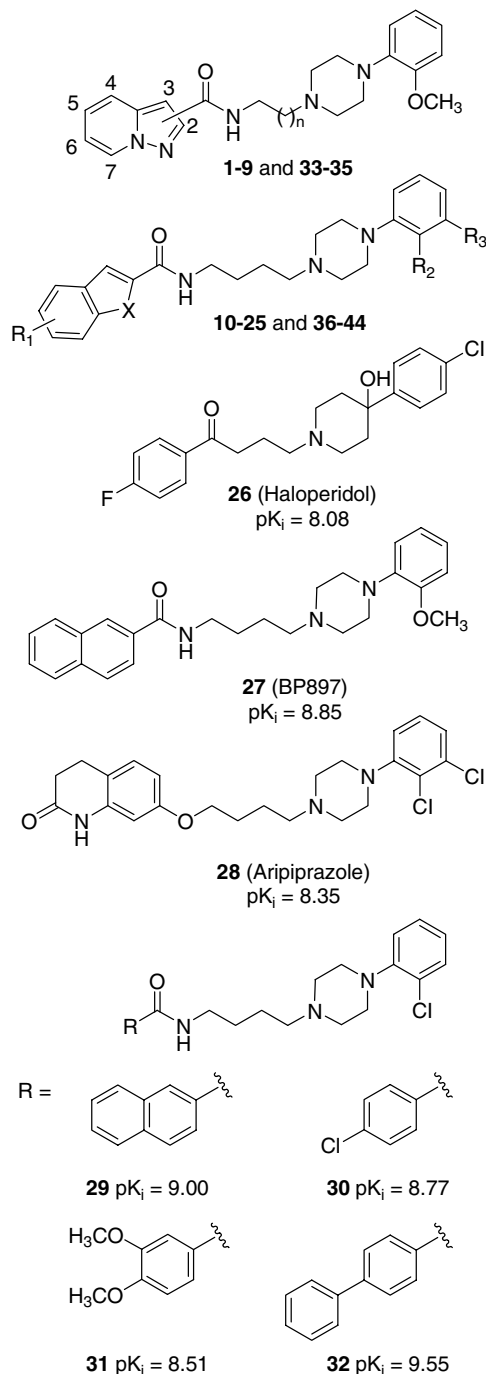
receptor binding, as well as to establish a working model that allows to facilitate further drug discovery efforts. In extension to previous 3D-QSAR analyses on D_4 antagonists¹⁹ and D_3 agonists,²⁰ we apply a well-established protocol on our training and test set comprising of 32 and 12 compounds, respectively. In addition to several techniques for monitoring the statistical quality and predictivity, we demonstrate the applicability of the resulting model in guiding synthetic efforts toward D_3 ligands with less flexible alkyl spacers. Thus, the study involved the prediction, synthesis, and biological testing of novel rigidized FAUC 365 analogues (45–47). Even though these molecules contain structural elements not directly represented in the training set, the good correspondence between the obtained experimental pK_i values and our previous predictions is encouraging.

As an extension to recent 3D-QSAR studies on D_3 ligands,^{21,22} a vital part of our modeling strategy was to enrich our dataset by a number of external reference ligands, such as haloperidol (26), BP 897 (27), and aripiprazole (28) thus enhancing the ligands' structural diversity. To ensure optimal comparability of the affinities for all ligands, we have obtained all receptor binding data used in this study within our laboratory.

2. Methods

2.1. Generation of structures and exploration of the conformational space

Structure building and refinement for the entire set of phenylpiperazine analogues (1–44, Scheme 1, Tables 1 and 2) was accomplished using SYBYL 6.9 molecular modeling software.²³ As templates for generating the whole series of phenylpiperazines with (hetero)arylcarb-



Scheme 1.

oxamide moiety, we have selected compounds 1, 2, 11, and 4, which are representatives for the ligands bearing an alkyl spacer of 2, 3, 4, and 5 atoms' length, respectively.

First, we performed a grid search, using the Tripos force field²⁴ with Gasteiger–Marsili charges,^{25,26} on the phenylpiperazine fragment, iterating the bond between piperazine and phenyl in steps of 30°. Afterwards, we accomplished full conformational analyses of the templates, while only the lowest energy conformer of phenylpiperazine was retained from the previous

Table 1. 2-Methoxyphenylpiperazines containing a pyrazolopyridine moiety in the training set (1–9) or in the test set (33–35) and their measured D₃ affinities¹⁶

Compound	Position	<i>n</i>	p <i>K</i> _i
<i>Training set</i>			
1	2	1	6.60
2	2	2	6.19
3	2	3	8.37
4	2	4	7.29
5	3	1	6.44
6	3	4	7.19
7	4	3	7.70
8	5	3	8.55
9	7	3	7.54
<i>Test set</i>			
33	3	3	7.74
34	3	2	6.82
35	6	3	8.37

Table 2. Substituted phenylpiperazines containing a heteroaromatic moiety in the training set (10–25) or in the test set (36–44) and their measured D₃ receptor affinities

Compound	X	R ₁	R ₂	R ₃	p <i>K</i> _i
<i>Training set</i>					
10 ^{a,b}	S	H	OCH ₃	H	9.63
11 ^{a,c}	S	H	Cl	Cl	9.30
12	S	5-CCH	OCH ₃	H	9.41
13 ^d	S	5-CN	OCH ₃	H	9.34
14	S	6-CCH	OCH ₃	H	9.42
15 ^a	O	H	OCH ₃	H	8.95
16 ^a	O	H	Cl	Cl	8.92
17 ^d	O	5-Br	OCH ₃	H	9.16
18 ^d	O	5-Br	Cl	Cl	8.46
19 ^d	O	5-CN	OCH ₃	H	8.37
20 ^d	N	H	Cl	Cl	9.18
21 ^d	N	5-CN	OCH ₃	H	9.24
22 ^d	N	5-Br	OCH ₃	H	9.61
23 ^d	N	6-CN	OCH ₃	H	9.60
24 ^d	N	5-Br	Cl	Cl	9.13
25 ^d	N	6-CN	Cl	Cl	9.45
<i>Test set</i>					
36 ^d	S	5-Br	OCH ₃	H	9.59
37 ^d	S	5-Br	Cl	Cl	8.49
38	S	5-CF ₃	OCH ₃	H	8.51
39	S	5-CF ₃	Cl	Cl	7.85
40	S	5-CCH	Cl	Cl	9.27
41 ^d	S	5-CN	Cl	Cl	9.60
42	S	6-CCH	Cl	Cl	9.24
43 ^d	S	6-CN	OCH ₃	H	9.48
44 ^d	S	6-CN	Cl	Cl	9.59

^a Ref. 16.^b FAUC 346.^c FAUC 365.^d Ref. 18.

calculation and kept fixed as an aggregate this time. The conformations for each template obtained from these analyses were separated into 8 to 17 conformational families employing a hierarchical clustering algorithm. The most reasonable low energy conformer was chosen from each of the obtained clusters. Using these four template structures, all other ligands of the corresponding series were derived by modification of

the (hetero)aromatic moiety and the phenylpiperazine substituents. The reference structures haloperidol (26) and aripiprazole (28) were constructed and their conformational space evaluated as described for the template structures. Finally, all ligands were optimized with MOPAC using a semiempirical AM1 Hamiltonian^{27,28} to improve the molecular geometries and ensure better comparability of the ligand structures by providing structures based on identical levels of calculation. The MMOK keyword was used in these calculations to ensure planar amide bonds.

2.2. Alignment

In general, the alignment is one of the most challenging aspects of 3D-QSAR. Thus, various approaches involving different degrees of complexity exist in order to address this problem. The spectrum of available techniques ranges from simple atom-based fitting procedures to sophisticated binding-site guided protocols. However, none of these has evolved to be superior over the others. In two recent 3D-QSAR investigations,^{19,20} we have found the ligand-based alignment technique ASP²⁹ to be very useful. Thus, we used the module ASP as implemented in the QSAR package TSAR,³⁰ which allows us to perform an alignment by comparison of steric overlap and molecular electrostatic potentials. For deriving reasonable electrostatic potentials, first, VESPA charges³¹ were calculated using the semiempirical program package VAMP.³² These atomcentered partial charges are obtained by a fit of the electronic wave function to the atomic positions. Compared to other charge schemes such as Coulson or Mulliken, they have the advantage that the anisotropy of the electron distribution around the molecule, especially for aromatic systems, is described in more detail.

As the basic template onto which the other ligands are to be superimposed, we have chosen FAUC 365, which shows considerably high dopamine D₃ receptor affinity. To quantify the relative orientation of two molecules, the combined similarity index based on the Carbo index for electrostatics and the shape similarity index to account for steric differences was evaluated (with both indices weighted equally) using three Gaussian functions for integration. This parameter was then optimized by overlaying the centroids of the molecules and performing a full translational and orientational search of each rigid comparison molecule relative to the lead compound FAUC 365 (11) by systematically rotating around the Cartesian *x*-, *y*-, and *z*-axes in 10° steps. For each new orientation, a Simplex algorithm in combination with Simulated Annealing directs the six degrees of freedom to an alignment with optimal similarity.²⁹ Finally, the orientation and placement of each ligand on the template 11 featuring the highest score related to this search algorithm was chosen to yield the TSAR-based alignment.

2.3. CoMFA and CoMSIA

To ensure best comparability between molecules, all pharmacological data of the ligands used in this study

have been measured within our laboratory. We performed a Comparative Molecular Field Analysis (CoMFA) evaluating the typically used steric and electrostatic fields implemented in SYBYL. All CoMFA calculations were accomplished using an sp^3 carbon atom with a charge of +1, a cutoff value of 30 kcal/mol for the Lennard-Jones and Coulomb-type potential, and a constant dielectric function. The dimension of the surrounding lattice (1.0 Å grid spacing) was selected with a sufficiently large margin to enclose all aligned molecules by at least 4 Å.

Putative problems of the analysis can arise from the absolute orientation of the molecules within the grid space.³³ A useful protocol to address this problem is the AOS/APS script of Wang et al.,³⁴ which automatically rotates/translates the entire dataset within the lattice without changing the relative orientation or alignment of the molecules. We applied the APS protocol varying the ligands by steps of 0.1 Å in all three dimensions within a 1.0 Å grid. After each of 1000 translational steps, the PLS analysis was repeated. This procedure gives detailed information about the translational dependence of the CoMFA, helps to ensure that no artificial effects are included, and provides evidence of the robustness of the model.

In the CoMSIA, all five physicochemical descriptors (electrostatic, steric, hydrophobic, and hydrogen-bond donor and acceptor) were evaluated using a common probe atom placed within a 3D grid. The atom was set up with a radius of 1.0 Å and charge, hydrophobic interaction, and hydrogen-bond donor and acceptor properties all equal to +1. Like in the CoMFA, the grid was extended beyond the molecular dimensions by 4.0 Å in the x , y , and z directions and the spacing between probe points within the grid was set at 1.0 Å. For the attenuation factor α controlling the steepness of the Gaussian function the standard value of 0.3 was accepted.

2.4. Partial least squares (PLS) analysis

The PLS method^{35,36} was used to linearly correlate the CoMFA and CoMSIA fields to biological activity values. The cross-validated analysis was performed using the leave-one-out (LOO) method in which one compound is removed and its activity is predicted using the model derived from the rest of the dataset. Complementing the results obtained from the leave-one-out cross-validation, the more robust leave-many-out procedure was performed to ensure the reproducibility of q^2 .³⁷ The cross-validated q^2 that resulted in minimal number of components and lowest standard error of prediction was accepted.^{38,39} To speed up the analysis and reduce noise, column filtering values (σ_{\min}) were iterated between 1.0 and 5.0 kcal/mol. Thus, only columns with a standard deviation of more than σ_{\min} were used for the cross-validation, resulting in approximately 5.5–15.6% of the original data to be used in the CoMFA and 4.1–12.7% used in the CoMSIA.

A final non-cross-validated analysis was performed using the optimal number of previously identified com-

ponents. After obtaining the models, the CoMFA and CoMSIA results were graphically interpreted by field contribution maps.

2.5. Calculation of the predictive correlation coefficient (r_{pred}^2) and prediction of novel compounds

The predictive ability of the 3D-QSAR model was determined from a set of 12 compounds (**33–44**) that were not included in the training set (Table 3). The compounds were manually assigned to the training or test set ensuring a reasonable range of pK_i units and structural diversity in both sets. These molecules were aligned using the same method as described before, and their activities were predicted using the model generated by the training set. Accompanying a synthetic strategy to design some rigidized analogues of the highly flexible ligands used in the training and test set, we also predicted three ligands (**45–47**) with cycloalkyl spacers, which were subsequently synthesized and tested. In addition to the classical test set, we also included these rigidized compounds in the calculation of r_{pred}^2 . Based on the test set molecules, this predictive correlation coefficient (r_{pred}^2) is defined as

$$r_{\text{pred}}^2 = (\text{SD} - \text{PRESS})/\text{SD};$$

where SD is the sum of the squared deviations of each biological property value from their mean and PRESS is the sum of squared differences between the predicted and actual affinity values for every molecule in test set.³⁶

3. Results and discussion

3.1. CoMFA

Using our properly selected training set of 32 D_3 ligands (Scheme 1 and Table 2), involving literature compounds with extended structural diversity such as haloperidol (**26**) and aripiprazole (**28**), we obtained statistically significant QSAR models (Table 4). The initial PLS analysis of our aligned training set applying a default σ_{\min} data filter of 2 kcal/mol yielded a cross-validated q^2 of 0.816 with $s_{c/v} = 0.432$ using two components (B). Increasing the minimum level of field variation σ_{\min} to purpose a more efficient reduction of noise, only a negligible further improvement of the statistics of the CoMFA model is found for $\sigma_{\min} = 3.0$ and 4.0 kcal/mol (C, D). Likewise, reduction of σ_{\min} to 1.0 kcal/mol shows also only negligible effects on the q_{cv}^2 (A). In contrast, increasing σ_{\min} further to 5.0 kcal/mol results even in a reduction of the cross-validated q^2 to 0.794 (E), which presumably reflects that some statistically relevant descriptors have been filtered out at this σ_{\min} value. With increasing σ_{\min} the number of remaining descriptors is noticeably decreased from 3603 to 1266, while at the same time the electrostatic contribution is raised from 27.7% to 36.1%. Thus, these results demonstrate that the obtained CoMFA is stable at a highly significant level (>0.8) and not prone to deviate noticeably with varying numbers of descriptors.

Table 3. Experimental and predicted biological affinities and residuals obtained by the CoMFA and CoMSIA model for 32 compounds in the training set and 15 compounds in the test set^a

Compound	p <i>K</i> _i (exp.)	p <i>K</i> _i (pred.)		Δp <i>K</i> _i	
		CoMFA	CoMSIA	CoMFA	CoMSIA
<i>Training set</i>					
1	6.60	6.450	6.252	0.150	0.348
2	6.19	7.208	7.181	-1.018	-0.991
3	8.37	8.689	8.690	-0.319	-0.320
4	7.29	7.621	7.152	-0.331	0.138
5	6.44	7.120	7.321	-0.680	-0.881
6	7.19	6.846	7.615	0.344	-0.425
7	7.70	8.110	8.330	-0.410	-0.630
8	8.55	8.586	8.304	-0.036	0.246
9	7.54	8.364	8.384	-0.824	-0.844
10	9.63	9.017	8.974	0.613	0.656
11	9.30	9.108	8.935	0.192	0.365
12	9.41	9.336	9.291	0.074	0.119
13	9.34	9.250	9.119	0.090	0.221
14	9.42	9.431	9.430	-0.011	-0.010
15	8.95	8.757	8.809	0.193	0.141
16	8.92	8.594	8.629	0.326	0.291
17	9.16	8.728	9.186	0.432	-0.026
18	8.46	9.136	9.178	-0.676	-0.718
19	8.37	9.069	9.222	-0.699	-0.852
20	9.18	9.098	9.118	0.082	0.062
21	9.24	9.430	9.369	-0.190	-0.129
22	9.61	9.243	9.246	0.367	0.346
23	9.60	9.371	9.324	0.229	0.279
24	9.13	9.418	9.709	-0.288	-0.579
25	9.45	9.309	9.046	0.141	0.404
26	8.08	7.690	7.590	0.390	0.490
27	8.85	8.918	9.123	-0.068	-0.273
28	8.35	8.433	7.498	-0.083	0.852
29	9.00	8.713	8.948	0.287	0.052
30	8.77	8.357	8.108	0.413	0.662
31	8.51	8.839	8.791	-0.329	-0.281
32	9.55	9.573	9.467	-0.023	0.083
<i>Test set</i>					
33	7.74	8.270	8.581	-0.530	-0.841
34	6.82	7.066	7.250	-0.246	-0.430
35	8.37	8.880	8.538	-0.510	-0.168
36	9.59	9.146	9.282	0.444	0.308
37	8.49	9.328	9.080	-0.838	-0.590
38	8.51	9.359	9.451	-0.849	-0.941
39	7.85	9.416	9.482	-1.566	-1.632
40	9.27	9.368	9.298	-0.098	-0.028
41	9.60	9.440	9.158	0.160	0.442
42	9.24	9.393	9.343	-0.153	-0.103
43	9.48	9.151	9.206	0.329	0.274
44	9.59	9.388	9.136	0.202	0.454
45	8.60	8.110	8.296	0.490	0.304
46	6.92	6.994	6.802	-0.074	0.118
47	6.85	7.036	7.329	-0.186	-0.479
<i>r</i> ² _{pred} ^b		0.651	0.613		

^a The experimental binding affinities toward the dopamine D₃ receptor are expressed as p*K*_i (-log*K*_i) values. Δp*K*_i is the error of cross-validated (training set) or predicted (test set) binding affinities and is defined as (p*K*_{i,experimental} - p*K*_{i,cross-validated/predicted}).

^b Predicted *r*² calculated with a standard deviation (SD) obtained from the test set only: 0.650 (CoMFA), 0.611 (CoMSIA).

Böhm et al., have attributed the dependence of *q*²_{cv} on the grid spacing and the absolute position of the aligned molecules within the lattice to the shape and steepness of the hyperbolic Lennard-Jones and Coulomb potentials

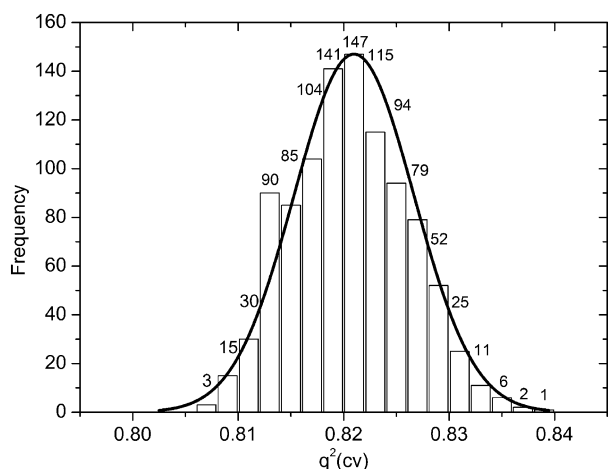
used during the analysis.⁴⁰ They stated that in the case of a 2.0 Å lattice, important contributions to the correlation analysis could be lost due to the required arbitrary cutoff values. Despite the fact that changing from a 2.0 to 1.0 Å lattice spacing results in an increase in computing time by a factor of 8, we performed all analyses using the smaller increment. Quantifying the translational dependence of *q*²_{cv} helps to ensure that no artificial effects are included in the final CoMFA and gives evidence of the robustness of the model. Thus, we applied a procedure published by Wang et al.,³⁴ which systematically translates the aligned dataset in space, followed by a PLS analysis after every retranslation. The histogram plot of the resulting 1000 model variants showed to be approximately corresponding to a normal distribution of the obtained *q*² values (Fig. 1). The highest *q*²_{cv} (0.839) was found for three components. Thus, it should be noted in this context that the increase of *q*²_{cv} values by less than 5% with the use of an additional component is regularly considered inappropriate due to the 'parsimony-principle'.⁴¹ However, what is even more interesting is the very narrow range of *q*²_{cv} values between 0.807 and 0.839 with 50% of the values lying between 0.817 and 0.825 indicating that our CoMFA model is considerably stable. Modification of other CoMFA parameters, such as changing the cutoff values for steric/electrostatic energies, did not give any improvement of the model. The final predicted/cross-validated versus experimental p*K*_i values for model B and their residuals (Δp*K*_i) are given in Table 3.

3.2. CoMSIA

In analogy to the CoMFA, already the initial PLS analysis of our aligned training set applying a default σ_{\min} data filter of 2.0 kcal/mol yielded a highly significant cross-validated *q*² of 0.741 with *s*_{cv} = 0.531 using four components (Table 4, G). Variation of the column filtering parameter σ_{\min} shows that for increasing σ_{\min} values from 1.0 to 5.0 kcal/mol, the number of descriptors is strongly reduced from 7309 to 2344, while the *q*²_{cv} is steadily increased from 0.738 (F) to 0.759 (J). Although the *q*² values of the CoMSIA models are slightly reduced compared to those of the CoMFA models, they are still indicating stable analyses of high quality. Furthermore, the CoMSIA models comprise valuable complementary information, as they offer additional explanation for the ligands' different receptor affinities by introducing three auxiliary field types, the hydrophobic field, the hydrogen bond acceptor field, and the hydrogen bond donor field. Interestingly, while the noise reduction in the CoMFA model decreased the fraction of the steric contribution from 72.3% down to 63.9%, it was increased by the noise reduction in the CoMSIA model from 10.9% up to 15.8%. The other CoMSIA field types typically contribute to the full model in the order: electrostatic (25.8–26.7%) > donor (22.2–23.5%) > acceptor (18.0–20.6%) > hydrophobic (17.3–19.3%). The final predicted/cross-validated versus experimental p*K*_i values for model G and their residuals (Δp*K*_i) are given in Table 3.

Table 4. Summary of the results from several PLS runs after applying different levels of noise reduction by column filtering (σ_{\min})

PLS run	CoMFA					CoMSIA				
	A	B	C	D	E	F	G	H	I	J
σ_{\min}	1	2	3	4	5	1	2	3	4	5
q_{cv}^2	0.815	0.816	0.818	0.820	0.794	0.738	0.741	0.744	0.751	0.759
s_{PRESS}	0.434	0.432	0.430	0.427	0.458	0.534	0.531	0.528	0.521	0.513
r^2	0.935	0.936	0.937	0.937	0.922	0.954	0.955	0.956	0.957	0.957
S	0.257	0.255	0.252	0.253	0.282	0.223	0.222	0.219	0.217	0.216
F	208.0	211.9	215.6	215.1	170.2	141.1	142.3	146.4	150.0	151.4
Components	2	2	2	2	2	4	4	4	4	4
Descriptors	3603	2305	1730	1433	1266	7309	5138	3891	3044	2344
<i>Fraction</i>										
Steric	0.723	0.704	0.671	0.645	0.639	0.109	0.109	0.118	0.138	0.158
Electrostatic	0.277	0.296	0.329	0.355	0.361	0.258	0.258	0.259	0.267	0.267
Hydrophob.						0.193	0.193	0.189	0.179	0.173
Donor						0.235	0.235	0.232	0.222	0.222
Acceptor						0.206	0.206	0.201	0.194	0.180

**Figure 1.** Histogram showing the distribution of q^2 values calculated by SAMPLS³³ leave-one-out cross-validation after systematic translation of aligned molecules within the lattice by an all placement search (APS).

3.3. Advanced cross-validation and assessment of model predictivity

Despite the good results obtained for CoMFA and CoMSIA cross-validation, of course, we are aware that there is always the danger to overemphasize the usefulness of cross-validation and q^2 as measures of the predictive performance. High values of q_{LOO}^2 can be regarded as a necessary, but not a sufficient, condition for a model to possess significant predictive power.⁴² Thus, we also performed the more critical and widely accepted leave-10%-out and leave-20%-out cross-validations. With $q_{L10\%}^2$ -values (mean \pm SD) of 0.812 ± 0.012 and 0.741 ± 0.018 for the CoMFA and CoMSIA, respectively, we have shown that even after discarding every tenth compound from the training set the predictivity of the models is hardly impaired. Repeating this calculation $n = 20$ times for each model assesses the liability of the respective model to random effects caused by different assignment of the ligands to the 10 groups. The negligible standard deviation (SD) is a further indicator of the model quality. Also the $q_{L20\%}^2$ -values of

0.799 ± 0.028 and 0.726 ± 0.038 for CoMFA and CoMSIA, respectively, show only a small decrease of the mean values, although disregarding every fifth compound. Likewise, there is only a marginal increase in the standard deviation. Therefore, we conclude that leave-10%-out and leave-20%-out cross-validation clearly corroborates the good stability and robustness of the models.

The predictive power of the CoMFA (PLS mode B) and CoMSIA (PLS mode G) analysis was further examined using a test set of 12 compounds (33–44, Scheme 1) that had been omitted from the training set. In addition to these test set ligands, we also included three rigidized compounds (45–47) in the calculation of the r_{pred}^2 value, which were synthesized accompanied by these QSAR predictions as described subsequently. The calculation was performed according to the formula of Cramer et al.,³⁶ and gave better results for the CoMFA with $r_{pred}^2 = 0.651$ than for the CoMSIA model with $r_{pred}^2 = 0.613$. The corresponding plots of the cross-validated or predicted versus the experimental binding affinities are shown for the training set (unfilled circles), the test set (filled circles), and the three newly synthesized compounds (filled triangles) in Figure 2.

3.4. Graphical interpretation of the fields

The three-dimensional representations of the CoMFA and CoMSIA field contributions as 'stdev*coeff' contour plots reveal where variability in the fields of the molecules is able to explain experimental binding differences. Thus, they can be useful to identify important features, which contribute to interactions between ligand and receptor in the active site.

3.4.1. CoMFA. Favored and disfavored cutoff energies were set at the 90th and 10th percentiles for the steric contributions and at the 85th and 15th percentiles for the electrostatic contributions, respectively. Because it is a representative example of the most active ligands, compound **22** is shown embedded as a guide into the steric (A) and electrostatic fields (C) (Fig. 3) resulting from a non-cross-validated CoMFA run ($\sigma_{\min} = 2.0$ kcal/

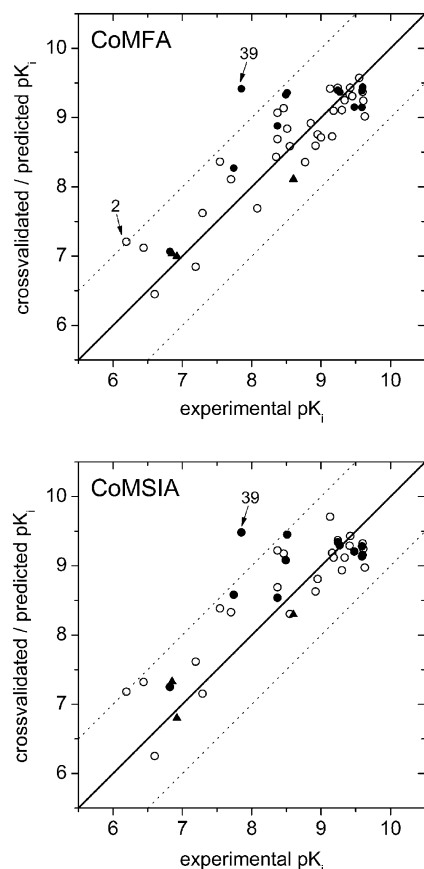


Figure 2. Fitted predictions versus experimental binding affinities for the 47 compounds in the training set (1–32: open circles) and the test set (33–44: filled circles/45–47: filled triangles). In addition to the line of ideal correlation, dotted lines are given, which indicate deviations from the actual pK_i by ± 1 logarithmic unit. Outliers are labeled by their compound numbers.

mol). Likewise, compound **6** is shown enclosed in the steric (B) and electrostatic fields (D) as a representative of lower affinity ligands. In panel (A), the green-colored regions specify areas where steric bulk enhances D_3 affinity, while the yellow contours mark regions where steric bulk leads to impaired biological activity. The predominant field color for the steric interactions in panel (A) is obviously yellow. This indicates that in several directions the tolerance for the displacement of structurally divergent ligands is rather limited, in order to avoid the occupation of any of those sterically forbidden yellow regions. The large yellow isopleths 1 and 2 below the phenylpiperazine reflect a strict decrease in affinity for all of these ‘anchor moieties’ being dislocated into this area. The other two larger yellow isopleth areas (3 and 4), which flank the sides of the indolecarboxamide, reveal that narrow (hetero)arylcarboxamides with a straight-lined orientation are preferentially recognized to yield high pK_i values, while any bent or perpendicular orientation, as well as sterically demanding systems, is detrimental for affinity (exemplified by **6** in (B)). In contrast, the green areas in position 5 and 6 of the indole of **22** indicate that substituents in these positions favor binding affinity to D_3 receptors. This, for instance, applies to the indole analogues **21–25**, which all bear a cyano or bromo substituent in position 5 or 6 and bind with subnanomolar affinity to the D_3 receptor.

In panel (B), the blue-colored regions show areas where electropositive charged groups enhance D_3 affinity, while in red regions groups with electronegative charges improve the receptor binding. The figure shows a blue area (1) in the vicinity of the protonated piperazine nitrogen. In consistency with the steric field, this blue isopleth suggests that the phenylpiperazine ‘anchor moiety’ should be fixed. Even small displacements, for example, in ligands with shorter spacers, are not well tolerated and lead to a substantial decrease of the pK_i . The

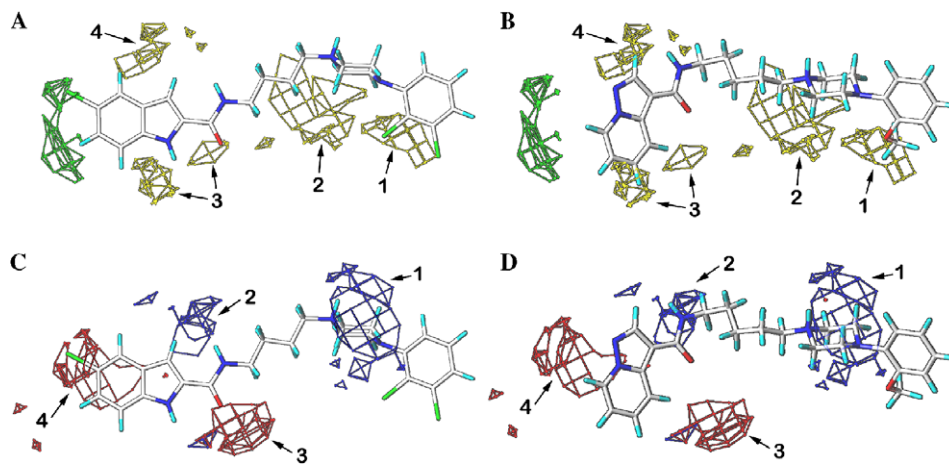


Figure 3. Stdev*coeff contour plots illustrating steric (A and B) and electrostatic features (C and D) as obtained by the final CoMFA. In (A) and (B), regions where steric bulk will enhance affinity are shown enclosed in green contours (contribution level⁵¹: 90%), whereas regions which should be kept unoccupied to prevent decrease of affinity are contoured in yellow (10%). This is exemplified by the high affinity ligand **22** ($pK_i = 9.61$) in (A) and the lower affinity ligand **6** ($pK_i = 7.19$) in (B). In (C) and (D), red contours (contribution level⁵¹: 15%) encompass regions where electron-rich fragments with negative partial charges will improve affinity. Blue contours (85%) indicate regions where reduced electron density (positive partial charges) is predicted to increase affinity. Again, compounds **22** (C) and **6** (D) are used to exemplify the plots for a high and lower affinity ligand, respectively.

blue contour 2 and the red contour 3 correspond exactly to the carboxamide function. Thus, different orientation or omission of this functional moiety exerts a negative impact on the binding properties as shown for **6** in panel (D). The electrostatic contour map shows a region of red polyhedrals (4) at position 6 and in particular at position 5 of the indole ring, indicating that electron-rich substituents are beneficial for the binding affinity. This field can be exemplified by the fact that the presence of the 5-cyano group in compounds **19** and **21**, the 6-cyano group in compounds **23** and **25**, and the 5-bromo group in compounds **17**, **18**, **22**, and **24**, gives rise to higher binding affinity than compounds (1–9).

3.4.2. CoMSIA. In Figure 4, as well as in the following discussion, the CoMSIA contour plots are exemplified

by ligands of low and high affinity. It becomes obvious from a direct comparison of Figures 3 and 4 that steric and electrostatic properties in CoMFA and CoMSIA show a high degree of similarity, however, a certain degree of complementary information can be found.

3.4.2.1. Steric contributions. In panel (A), green and yellow isopleths are drawn at a contribution level of 90% and 10%, and enclose regions favorable or unfavorable for bulky groups, respectively.

As in the CoMFA, the only green isocontour (1) found in Figure 4A and B is located most distant to the phenyl-piperazine on the far left side. It can be occupied, for example, by the terminal ring of the biphenyl in **32** (B) or by the six-membered ring of the heteroaromatic

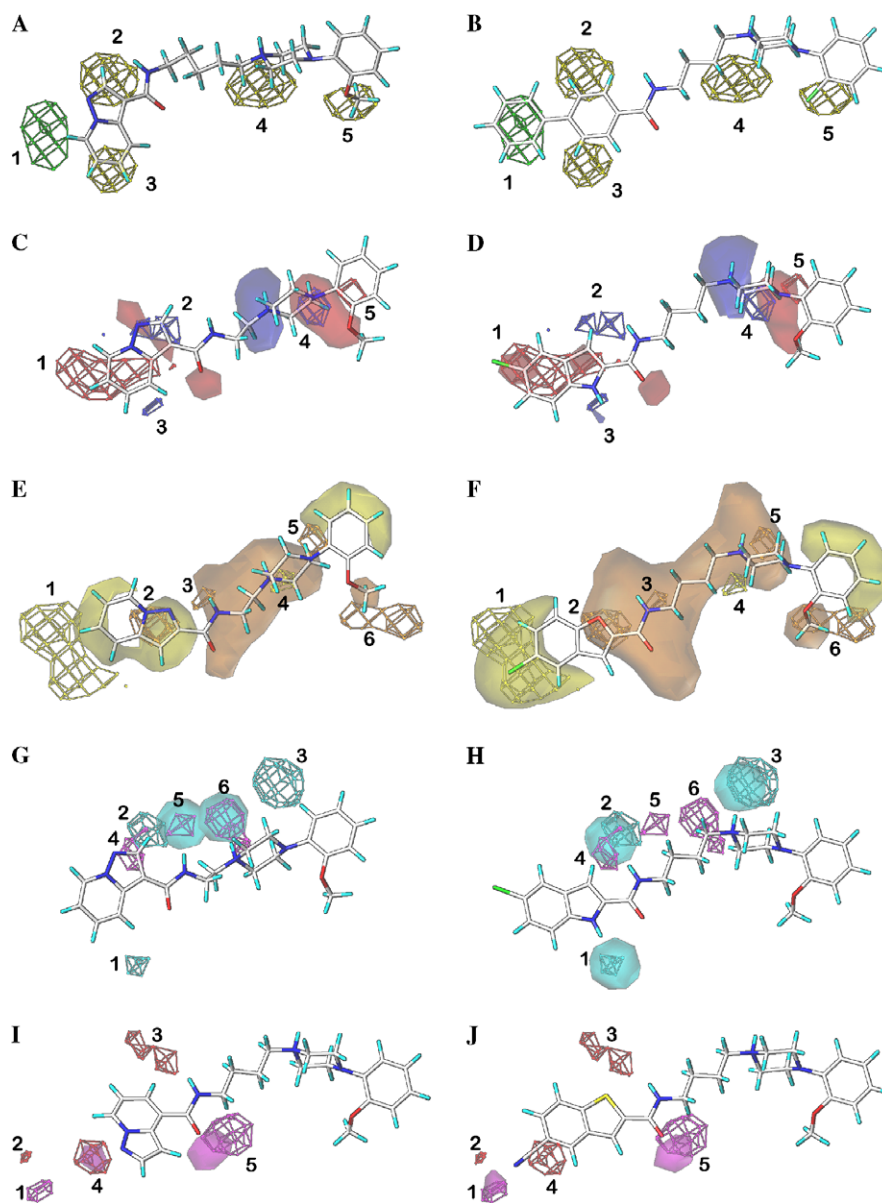


Figure 4. Stdev*coeff contour plots illustrating steric (A + B), electrostatic (C + D), hydrophobic (E + F), and hydrogen bond donor (G + H) and acceptor (I + J) properties revealed by the final CoMSIA. For all features, one ligand with low (A: **6**, C: **5**, E: **1**, G: **5**, I: **7**) and another with high affinity (B: **32**, D: **22**, F: **17**, H: **22**, J: **13**) are shown in comparison. The mesh fields represent the stdev*coeff plots, whereas the transparent surfaces indicate the fields of the particular ligand, thus, facilitating the recognition of matching or mismatching features.

system of those active ligands, which contain a butylene spacer and the carboxamide function in position 2 of the benzothiophene, benzofuran or indole nucleus. In contrast, for ligands containing a spacer of different length or the carboxamide function in a different position of the heterocycle, such as **6**, the green isopleth is not even touched (A). However, **6** as an example of a bend ligand penetrates the forbidden regions 2 and 3 much more than straight ligands, such as **32**, do. As in the CoMFA, the isopleths 4 and 5 below the phenylpiperazine partial structure penalize any displacement of this 'anchor region'. Isopleth 5 can also be explained by a number of low affinity ligands (pyrazolopyridine derivatives) bearing an *ortho*-methoxy substituent in this region.

3.4.2.2. Electrostatic contributions. Red and blue isopleths (contribution level 90%/20%) enclose regions favorable for negative and positive charge, respectively. A large, red isopleth (1) is located at the π -system of the left-sided heterocyclic or isocyclic ringsystems of ligands showing high D_3 affinity (Fig. 4D). While, for example, the indole nucleus of **22** (panel (D)) is able to place its negative electrostatic fields (transparent red) perfectly within this mesh, the pyrazolo[1,5-*a*]pyridine nucleus of **5** (panel (C)) fails to do so. Above and below the extended red mesh, the blue areas 2 and 3 indicate where electron-deficient substructures should be placed. These two areas reflect a common placement of the carboxamide hydrogens (2) of the highly potent ligands and the indole hydrogen (3), respectively. The blue isopleth 4 exhibits the influence of the protonated piperazine nitrogen (N_1) for the active ligands, while the red one (5) arises from the electron rich, tertiary piperazine nitrogen (N_2) of those compounds. Consequently, these two isopleths determine the preferred position of the piperazine ring, which is of course affected by the number of carbons in the alkyl chain. Thus, Figure 4 shows that the piperazine moiety of **5** is misplaced (panel (C)), because of the short two-carbon atom spacer (the blue isopleth 4 is completely buried in the transparent red electrostatic potential at the N_2 of the piperazine).

3.4.2.3. Hydrophobic contributions. Yellow and orange isopleths (contribution level 85%/15%) enclose regions favorable for hydrophobic and hydrophilic groups, respectively. The yellow mesh 1 encloses the 4, 5, and 6 positions of the heterocyclic rings, which can be ascribed, for example, to the 5-bromo-substitution of several potent compounds (**17**, **18**, **22**, and **24**). As exemplified in panel (F) for **17**, a bromo substituent enhances the size of the molecular hydrophobic field (transparent yellow) significantly compared to an unsubstituted heteroaromatic moiety as shown in **1** (panel (E)). The heteroatoms within the bicyclic moieties of the active ligands and the carboxamidic hydrogens are responsible for the orange isopleths 2 and 3, respectively. The N_1 piperazine nitrogen of the low affinity compounds (such as **1**) is lying adjacent to the yellow isosurface 4, while that of the active structures corresponds to the orange one (5). In addition, exactly this area 5 is not enclosed in the large, hydrophilic molecular field (transparent orange) of ligand **1**, as a representative of weak D_3 receptor binding. The hydrophilic field

(transparent orange) induced by the methoxy group of several potent ligands (**10**, **12**, **13**, **14**, **15**, **17**, **19**, **21**, **22**, and **23**) overlaps the orange isopleth 6.

3.4.2.4. Hydrogen bond donor contributions. Cyan contour maps (contribution level 75%) are representing the position of H-bond donor groups which favor biological activity, while purple areas (10%) are outlining the location of biologically unfavored donors.

The cyan isocontours 1, 2, and 3 result from the indole-NH (ligands **20–25**), from the carboxamide moiety, and from the protonated piperazine nitrogen N_1 . These maps can be occupied only by ligands showing good D_3 affinity (butylene-spacer required), such as **22** (panel (H)), while less active compounds (in particular with ethyl or propyl spacer) point toward the unfavored purple areas 4, 5, and 6, as exemplified by **5** in panel (G). It should be noted that map 3 might be equivalent to Asp3.32, which is responsible for forming a 'reinforced ionic bond' (consisting of a H-bond-mediated and an ionic electrostatic interaction) to the protonated piperazine within in the D_3 -pocket.

3.4.2.5. Hydrogen bond acceptor contributions. Magenta isopleths (90%) encompass regions where a hydrogen bond acceptor will lead to improved biological activity, while an acceptor located near the red regions (10%) will result in impaired biological activity.

The 5- or 6-cyano group (H-bond acceptor) within the active ligands **13** (panel (J)), **23**, and **25** exhibits a perfect fit to the magenta isopleth 1. Compound **19** also bears a 5-cyano substituent. However, as its heteroaromatic moiety is flipped horizontally within the alignment, the cyano function points toward the red map 2, which offers an explanation for the worse biological data of **19**. The red mesh 3 reveals the low activity of the 2-substituted pyrazolopyridines, because their acceptor nitrogen is typically located in close proximity. The reduced affinity of **7** (panel (I)) can be explained in part by its molecular acceptor field (transparent magenta), which corresponds to the pyrazolopyridine nitrogen, being completely embedded in the unfavorable red mesh 4. The carboxamide oxygens of various, highly potent ligands align to a common position close to the magenta isopleth 5, while, for instance, the low affinity compound **2** is not able to place its carbonyl oxygen in this region.

3.5. Prediction of novel, rigidized compounds

After establishing and evaluating our 3D-QSAR models, we were intrigued by the question, whether we can employ them also for the prediction of novel compounds containing structural elements hitherto unrepresented by any other ligand in the training or test set.

Rigidization is a classic and popular strategic concept in modern medicinal chemistry. Its objective is to synthetically fix a flexible ligand scaffold in a biologically relevant conformation with both implications on the enthalpy and entropy of binding to a biological target. Thus, we envisioned to exchange the flexible butylene

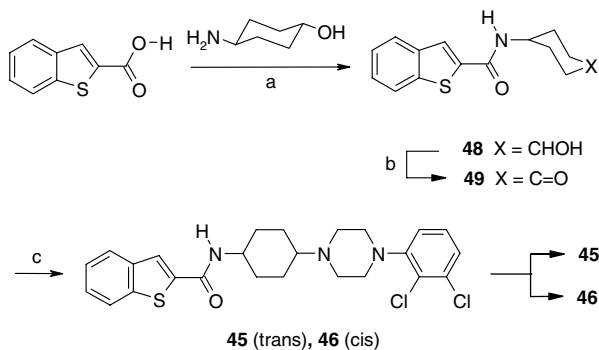
spacer of the highly potent and selective D₃ ligand FAUC 365 (**11**) by a conformationally restricted bioisostere. The first strategy was to replace the butylene by a 1,4-cyclohexylene spacer, which could provide a *trans* or a *cis* configuration between the benzothiophenyl carboxamide and the 2,3-dichlorophenylpiperazine. The second strategy involved replacement of the butylpiperazine by an ethyl-octahydro-2*H*-pyrido[1,2-*a*]pyrazine. When the test compounds (**45–47**) were predicted employing the CoMFA and CoMSIA models, the *trans*-cyclohexyl derivative **45** was suggested to bind to the D₃ receptor with nanomolar affinity ($pK_i = 8.11/8.30$ predicted from CoMFA/CoMSIA). The *cis*-cyclohexyl derivative **46** and the ethyl-octahydro-2*H*-pyrido[1,2-*a*]pyrazine derivative **47**, in contrast, were supposed to give lower D₃ affinities ($pK_i^{\text{CoMFA/CoMSIA}} = 7.00/6.80$ predicted for **46** and $7.04/7.33$ for **47**, respectively).

Subsequently, we have proceeded with the synthesis of all three novel ligands in order to verify or falsify our predictions and, thus, to further evaluate, whether we can challenge our models by predicting structurally diverging ligands.

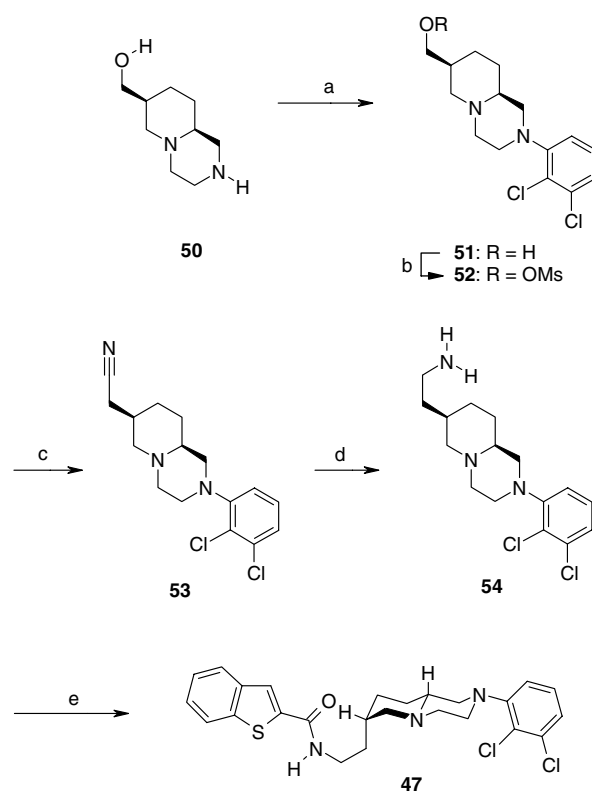
3.6. Chemistry

For the synthesis of the diastereomeric target compounds **45** and **46** (Scheme 2), we started from commercially available benzo[*b*]thiophene-2-carboxylic acid and *trans*-4-aminocyclohexanol employing activation with TBTU to yield the carboxamide **48**. Subsequent oxidation with the mild hypervalent iodine reagent IBX resulted in formation of the corresponding ketone **49**. Finally, reductive amination with 1-(2,3-dichlorophenyl)piperazine yielded in a mixture of regioisomers **45** and **46**. Separation of the isomers was accomplished by flash chromatography to give the *trans*- and *cis*-isomers **45** and **46**, respectively.

Following a five-step protocol⁴³ we prepared the bicyclic system **50** as a chiral building block (Scheme 3). A synthetic route to the intermediate **51** was elaborated



Scheme 2. Reagents and conditions: (a) TBTU, DIPEA, DMF, CH₂Cl₂, 0 °C to rt, 1 h (64%); (b) IBX, DMSO, rt, 1 h (56%); (c) Na(OAc)₃BH, 2,3-dichlorophenylpiperazine, 1,2-dichloroethane, rt, 3.5 h (84%); flash chromatography, CH₂Cl₂–MeOH, 98:2, (**45**: 22%; **46**: 14%).

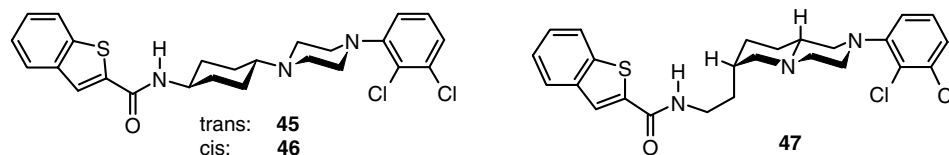


Scheme 3. Reagents and conditions: (a) 1-bromo-2,3-dichlorobenzene, Pd₂(dba)₃, BINAP, NaOH-*t*-Bu, toluene, 80 °C, 2.5 h (51%); (b) MsCl, Et₃N, THF, –30 °C to rt, 0.5 h (71%); (c) Bu₄NCN, DMSO, 80 °C, 8 h (77%); (d) LiAlH₄, Et₂O, 0 °C to rt, 1 h (66%); (e) benzo[*b*]thiophene-2-carboxylic acid, TBTU, DIPEA, DMF, CH₂Cl₂, 0 °C to rt, 1 h (71%).

when we took advantage of a Buchwald–Hartwig cross coupling^{44,45} as a key reaction step. Thus, palladium promoted amination of 1-bromo-2,3-dichlorobenzene with the bicyclic skeleton **50** gave the *N*-aryl substituted pyridopyrazine **51**. Subsequent treatment with methanesulfonyl chloride yielded **52**. Nucleophilic substitution with tetrabutylammonium cyanide resulted in formation of the nitrile **53**, which could be reduced with LiAlH₄ to furnish the primary amine **54**. Finally, coupling with benzo[*b*]thiophene-2-carboxylic acid was induced by TBTU to provide the final product **47**.

3.7. Biological testing

Receptor binding experiments were established to evaluate the binding properties of the target compounds **45–47** in comparison to the reference agents BP 897 and FAUC 365 (Table 5). The obtained experimental results showed to be in very good consistency with our previous CoMFA/CoMSIA predictions (Table 3). All deviations were found to be below 0.5 p*K*_i units. In fact, the *trans*-cyclohexyl derivative **45** displayed considerably higher D₃ affinity (*K*_i = 2.5 nM) than its *cis* analogue **46** or the bicyclic derivative **47**. While being only moderately selective for D₃ over 5-HT_{1A} or D₂ receptors, selectivity over the antitarget α₁ was substantial. Besides a large selectivity over D₁ and 5-HT₂, **45** showed a pro-

Table 5. Receptor binding data of **45–47** compared to the reference compounds BP 897 (**27**) and FAUC 365 (**11**) utilizing human D2_{long}, D2_{short}, D3, and D4.4 receptors as well as porcine D1, 5-HT_{1A}, 5-HT₂, and α_1 receptors^a

Compound	K_i values in (nM)								
	³ H]SCH 23390		³ H]spiperone				³ H]8-OH-DPAT	³ H]ketan serin	³ H]prazosin
	D1	D2 _{long}	D2 _{short}	D3	D4.4	5-HT _{1A}	5-HT ₂	α_1	
45	4300	76	78	2.5	8000	47	8900	240	
46	2200	2900	2600	120	460	810	18000	85	
47	990	490	1100	140	180	230	1200	49	
FAUC 365 (11)	8800	3600	2600	0.50	340	360	3000	370	
BP 897 (27)	760	220	200	1.3	44	81	840	5.0	

^a K_i values in nM are based on the means of 2–5 experiments each done in triplicate.

nounced, about 3200-fold, selectivity over D₄ receptors, which was superior to both reference ligands, BP 897 and FAUC 365. In contrast to the interesting pharmacological receptor binding profile of **45**, the *cis* analogue **46** and the bicyclic derivative **47** bind only with moderate affinities to the D₃ receptor ($K_i = 120$ and 140 nM, respectively), as we have predicted it. Indeed, they showed even higher affinities for the α_1 receptor subtype.

4. Conclusion

In the current work, we have successfully established CoMFA and CoMSIA models based on a training set of 32 ligands. We have carefully evaluated the statistical significance of the models and found high q_{cv}^2 values of 0.82 (2 components) and 0.76 (4 components) for CoMFA and CoMSIA, respectively, when using the standard leave-one-out cross-validation method. Even for the more critical leave-20%-out method, q_{cv}^2 was only slightly reduced yielding still highly significant mean values ($n = 20$ runs) of 0.80 for CoMFA and 0.73 for CoMSIA. The models were verified to be stable and robust against the variation of the underlying parameters. Thus, an all placement search (APS) yielded only CoMFA models in the rather narrow range between 0.807 and 0.839. Using a test set of 12 ligands, we were able to demonstrate that the models are also predictive for new compounds. This was extended to the successful application of our models guiding the synthesis of novel, rigidized derivatives (**45–47**). Thus, we have discovered a new bioactive agent (**45**) with decreased flexibility by introduction of a *trans*-cyclohexyl spacer. In addition to good D₃ affinity, the test compound **45** exhibited improved (~3200-fold) selectivity over D₄ receptors.

The theoretical investigations presented in this study provide a valuable tool for predicting the affinity of novel compounds and, thus, for guiding and evaluating further structural modifications.

5. Experimental

5.1. Methods and materials

Chemicals and solvents were purchased in highest purity available. All reactions were carried out under nitrogen atmosphere. Column chromatography was performed using 60 μ m silica gel from Merck. For TLC silica gel 60 F₂₅₄ plates from Merck were used (UV, I₂ or ninhydrin detection). Melting temperatures were determined on a Buechi 510 apparatus and are uncorrected. NMR data were acquired on a Bruker AM-360 or Bruker AVANCE 360 MHz spectrometer. Chemical shifts are noted in ppm relative to TMS. IR spectroscopy was carried out on a Jasco FT/IR 410 spectrometer. EI-MS was performed on a Finnigan MAT TSQ 70 spectrometer. Molecular modeling investigations were performed on a Silicon Graphics Indigo2 and Octane2 workstation.

5.2. Benzo[*b*]thiophene-2-carboxylic acid 4-hydroxycyclohexyl amide (**48**)

To a solution of benzo[*b*]thiophene-2-carboxylic acid (purchased from Acros Organics, Belgium) (0.28 g, 1.20 mmol) and DIPEA (0.70 mL, 4.80 mmol) in CH₂Cl₂ (10 mL) was added TBTU (0.42 g, 1.30 mmol) in DMF (4 mL) at 0 °C. After addition of *trans*-4-aminocyclohexanol (0.17 g, 2.60 mmol) (purchased from Acros Organics, Belgium) in CH₂Cl₂ (5 mL), the mixture was stirred at room temperature for 1 h. Then, CH₂Cl₂ and aqueous saturated NaHCO₃ were added. The combined organic layers were dried (MgSO₄) and evaporated, and the residue was purified by flash chromatography (CH₂Cl₂–MeOH 98:2) to give benzo[*b*]thiophene-2-carboxylic acid 4-hydroxycyclohexyl amide (0.21 g, 64%) as a white solid. Mp 220–222 °C. ¹H NMR (CDCl₃, 360 MHz): δ 1.30–1.55 (m, 4H), 2.00–2.09 (m, 2H), 2.10–2.20 (m, 2H), 3.64–3.71 (m, 1H), 3.97–3.99 (m, 1H), 5.85–5.87 (m, 1H), 7.38 (ddd, $J = 0.3$ Hz, 5.0 Hz, 8.0 Hz, 1H), 7.40–7.43 (m, $J = 0.3$ Hz, 5.0 Hz, 8.0 Hz, 1H), 7.76 (d, $J = 0.1$ Hz), 7.80–7.86 (m, 2H). ¹³C NMR (CDCl₃, 90 MHz): δ

30.9, 33.9, 55.3, 69.8, 122.7, 124.9, 125.0, 125.2, 126.7, 138.5, 139.1, 140.7, 161.6. IR (NaCl): 3385, 3321, 2925, 2852, 1621 cm^{-1} . EI-MS m/z : 275 M^+ . Anal. ($\text{C}_{15}\text{H}_{17}\text{NO}_2\text{S}$) C, H, N.

5.3. Benzo[*b*]thiophene-2-carboxylic acid 4-oxocyclohexyl amide (49)

To a solution of benzo[*b*]thiophene-2-carboxylic acid 4-hydroxycyclohexyl amide (0.10 g, 0.36 mmol) was added IBX ((1-hydroxy-1,2-benziodoxol-3(1*H*)-on-1-oxide) 0.12 g, 0.43 mmol) in dry DMSO (4 mL) and stirred at rt for 1 h. Then, Et_2O and aqueous saturated NaHCO_3 were added. The organic layer was dried (MgSO_4) and evaporated to yield in benzo[*b*]thiophene-2-carboxylic acid 4-oxocyclohexyl amide (60.0 mg, 56%) as a white solid. Mp 185–188 °C. ^1H NMR (CDCl_3 , 360 MHz): δ 1.75–1.78 (m, 2H), 1.83–1.86 (m, 2H), 2.33–2.41 (m, 2H), 2.44–2.56 (m, 2H), 4.43–4.46 (m, 1H), 6.16–6.18 (m, 1H), 7.38 (ddd, $J = 0.3$ Hz, 5.0 Hz, 8.0 Hz, 1H), 7.42 (ddd, $J = 0.3$ Hz, 5.0 Hz, 8.0 Hz, 1H), 7.78 (d, $J = 0.3$ Hz, 1H), 7.80–7.87 (m, 2 H) ^{13}C NMR (CDCl_3 , 90 MHz): δ 32.1, 39.1, 47.2, 122.7, 125.0, 125.5, 126.5, 138.0, 139.0, 140.8, 161.9, 209.1. IR (NaCl): 3313, 2942, 2852, 1716, 1625 cm^{-1} . EI-MS m/z : 273 (M^+). Anal. ($\text{C}_{15}\text{H}_{15}\text{NO}_2\text{S} \cdot 0.16\text{H}_2\text{O}$) C, H, N.

5.4. *N*-[4-[4-(2,3-Dichlorophenyl)piperazin-1-yl]cyclohexyl]benzo[*b*]thiophene-2-carboxamide (45 + 46)

To a solution of benzo[*b*]thiophene-2-carboxylic acid 4-oxocyclohexyl amide (0.60 mg, 0.21 mmol) and $\text{Na}(\text{OAc})_3\text{BH}$ (60.0 mg, 0.28 mmol) in dry $\text{C}_2\text{H}_5\text{Cl}_2$ (5 mL) was added 1-(2,3-dichlorophenyl)piperazine (0.10 g, 0.42 mmol) and stirred at rt for 3.5 h. After addition of Et_2O and aqueous saturated NaHCO_3 , the aqueous layer was extracted with CH_2Cl_2 . The combined organic layers were dried (MgSO_4) and evaporated, and the residue was purified by flash chromatography (CH_2Cl_2 –MeOH 98:2) to give *N*-[4-[4-(2,3-dichlorophenyl)piperazine-1-yl]cyclohexyl]benzo[*b*]thiophene-2-carboxamide as a mixture of *cis*-, *trans*-isomers (64.0 mg, 84%).

5.4.1. *trans*-*N*-[4-[4-(2,3-Dichlorophenyl)piperazin-1-yl]cyclohexyl]benzo[*b*]thiophene-2-carboxamide (45). The mixture of isomers was purified another time by flash chromatography (CH_2Cl_2 –MeOH 97:3) yielding in the pure *trans*- (14.0 mg, 22% of the mixture) and *cis*-isomer (9.00 mg, 14%). Mp 266–268 °C. ^1H NMR (CDCl_3 , 360 MHz): δ 1.35 (m, 4H), 2.06–2.08 (m, 2H), 2.25–2.28 (m, 2H), 2.40–2.43 (m, 1H), 2.79–2.80–2.83 (m, 4H), 3.10–3.13 (m, 4H), 3.96–3.99 (m, 1H), 5.92–5.94 (m, 1H), 6.99–7.05 (m, 1H), 7.13–7.16 (m, 2H), 7.37–7.44 (m, 2H), 7.75 (s, 1H), 7.81–7.86 (m, 2H). ^{13}C NMR (CDCl_3 , 90 MHz): δ 27.3, 32.3, 49.1, 49.3, 51.8, 62.7, 118.6, 122.7, 124.5, 124.9, 125.0, 125.1, 126.3, 127.4, 127.5, 134.0, 138.6, 139.1, 140.7, 151.3, 161.5. IR (NaCl): 3274, 3060, 2944, 2801, 2762, 1620 cm^{-1} . EI-MS m/z : 487, 489 (M^+). Anal. ($\text{C}_{25}\text{H}_{27}\text{Cl}_2\text{N}_3\text{OS}$) C, H, N.

5.4.2. *cis*-*N*-[4-[4-(2,3-Dichlorophenyl)piperazin-1-yl]cyclohexyl]benzo[*b*]thiophene-2-carboxamide (46). As de-

scribed before the mixture of isomers was purified another time by flash chromatography (CH_2Cl_2 –MeOH 97:3) yielding in the pure *trans*- (14.0 mg, 22% of the mixture) and *cis*-isomer (9.00 mg, 14%). Mp 140–143 °C. ^1H NMR (CDCl_3 , 360 MHz): δ 1.64–2.02 (m, 8H), 2.31–2.36 (m, 1H), 2.74–2.78 (m), 3.08–3.11 (m, 4H), 4.22–4.29 (m, 1H), 6.16–6.19 (m, 1H), 6.95–6.98 (m), 7.14–7.16 (m, 2H), 7.39–7.44 (m, 2H), 7.76 (s, 1H), 7.80–7.86 (m, 2H). ^{13}C NMR (CDCl_3 , 90 MHz): δ 15.2, 25.2, 28.6, 49.8, 51.5, 65.8, 118.5, 122.7, 124.6, 124.9, 125.0, 125.1, 126.3, 127.4, 127.5, 134.1, 138.8, 139.1, 161.5. IR (NaCl): 3274, 3060, 2944, 2801, 2762, 1620 cm^{-1} . EI-MS m/z : 487, 489 (M^+) HREIMS calcd for $\text{C}_{25}\text{H}_{27}\text{Cl}_2\text{N}_3\text{OS}$: 487.1252. Found: 487.1249 (M^+).

5.5. [(7*S*,9*aS*)-2-(2,3-Dichlorophenyl)octahydropyrido[1,2-*a*]pyrazine-7-yl]methanol (51)

[(5*S*,7*S*)-1-(Octahydropyrido[1,2-*a*]pyrazine-7-yl)methanol⁴³ was synthesized according to Ref. 43. To a suspension of [(5*S*,7*S*)-1-(octahydropyrido[1,2-*a*]pyrazine-7-yl)methanol (0.50 g, 2.90 mmol), 1-bromo-2,3-dichlorobenzene (0.55 g, 2.50 mmol), $\text{Pd}_2(\text{dba})_3$ (22.5 mg, 0.50 mol%), and BINAP ((±)-2,2'-bis(diphenylphosphino)-1,1'-binaphthyl; 45.0 mg 2 mol%) in toluene (8 mL) was added $\text{NaOH}t\text{-Bu}$ (1.00 g, 12.0 mmol). The reaction mixture was heated for 2.5 h to 80 °C, cooled to room temperature, filtered through Celite, and evaporated, yielding [(7*S*,9*aS*)-2-(2,3-dichlorophenyl)octahydropyrido[1,2-*a*]pyrazine-7-yl]methanol (0.47 g, 51%) as a yellow oil. ^1H NMR (CDCl_3 , 360 MHz): δ 1.58–1.56 (m, 1H), 1.69–1.91 (m, 4H), 2.34 (br dd, $J = 10.3$ Hz, 10.3 Hz, 1H), 2.48 (ddd, $J = 2.5$ Hz, 11.3 Hz, 11.3 Hz, 1H), 2.49–2.52 (m, 1H), 2.53 (dd, $J = 10.6$ Hz, 10.6 Hz, 1H), 2.88 (ddd, $J = 2.5$ Hz, 5.2 Hz, 11.3 Hz, 1H), 2.92 (dd, $J = 2.7$ Hz, 11.4 Hz, 1H), 3.01 (br d, $J = 11.6$ Hz, 1H), 3.23 (ddd, $J = 2.6$ Hz, 2.6 Hz, 10.6 Hz, 1H), 3.31 (br dd, $J = 2.7$ Hz, 11.4 Hz, 1H), 3.89 (ddd, $J = 1.4$ Hz, 3.4 Hz, 10.4 Hz, 1H), 4.02 (dd, $J = 4.5$ Hz, 10.4 Hz, 1H), 6.95 (m, 1H), 7.14–7.20 (m, 2H). ^{13}C NMR (CDCl_3 , 90 MHz): δ 26.6, 27.5, 34.2, 51.4, 55.2, 57.3, 58.5, 61.0, 68.6, 118.5, 124.6, 127.4, 127.5, 134.2, 151.0. IR (NaCl): 3379, 2924, 2853, 2824, 1578 cm^{-1} . EI-MS m/z : 314, 316 (M^+).

5.6. [(7*S*,9*aS*)-2-(2,3-Dichlorophenyl)octahydropyrido[1,2-*a*]pyrazine-7-yl] methyl-sulfonate (52)

[(7*S*,9*aS*)-2-(2,3-Dichlorophenyl)octahydropyrido[1,2-*a*]pyrazine-7-yl]methanol (0.20 g, 0.65 mmol) was dissolved in dry THF (4 mL), cooled to –30 °C. Then were added Et_3N (0.14 mL, 0.97 mmol) and methanesulfonyl chloride (0.08 mL, 6.00 mmol). The reaction mixture was stirred at room temperature for 30 min, filtered through Celite, and evaporated, yielding [(7*S*,9*aS*)-2-(2,3-dichlorophenyl)octahydropyrido[1,2-*a*]pyrazine-7-yl] methyl-sulfonate (0.18 g, 71%) as a white solid. Mp 110–112 °C. ^1H NMR (CDCl_3 , 360 MHz): δ 1.36 (ddd, $J = 3.5$ Hz, 10.6 Hz, 13.6 Hz, 1H), 1.48 (dddd, $J = 2.5$ Hz, 3.5 Hz, 3.5 Hz, 13.6 Hz, 1H), 1.68 (dddd, $J = 4.8$ Hz, 4.8 Hz, 13.9 Hz, 13.9 Hz, 1H), 1.86 (dddd, $J = 1.6$ Hz, 1.6 Hz, 2.7 Hz, 13.9 Hz, 1H), 2.17–2.30 (m, 1H), 2.27 (ddd, $J = 2.7$ Hz, 10.3 Hz, 10.6 Hz, H-4_a),

2.36 (dd, $J = 3.4$ Hz, 11.8 Hz, 1H), 2.49 (ddd, $J = 2.9$ Hz, 11.3 Hz, 11.3 Hz, 1H, H-6_a), 2.51 (dd, $J = 10.2$ Hz, 10.7 Hz, 1H), 2.74 (ddd, $J = 2.4$ Hz, 2.4 Hz, 11.3 Hz, 1H, H-6_e), 2.86 (ddd, $J = 1.8$ Hz, 1.8 Hz, 12.0 Hz, 1H), 2.89 (ddd, $J = 2.6$ Hz, 11.4 Hz, 11.4 Hz, 1H), 3.06 (s, 3H), 3.16 (ddd, $J = 2.6$ Hz, 2.6 Hz, 10.7 Hz, 1H), 3.25 (ddd, $J = 2.6$ Hz, 2.6 Hz, 11.4 Hz, 1H), 4.40 (dd, $J = 7.5$ Hz, 9.5 Hz, 1H), 4.51 (dd, $J = 7.5$ Hz, 9.5 Hz, 1H), 6.96 (dd, $J = 3.2$ Hz, 6.4 Hz, 1H), 7.14–7.19 (m, 2H). ¹³C NMR (CDCl₃, 90 MHz): δ 24.3, 24.8, 33.5, 37.1, 51.3, 54.95, 55.6, 57.1, 61.1, 71.1, 118.5, 124.6, 127.4, 127.5, 134.0, 151.1. IR (NaCl): 2929, 2818, 2774, 1578, 1450, 1244, 1355, 1174 cm⁻¹. EI-MS m/z : 392, 394 (M⁺).

5.7. [(7*S*,9*aS*)-2-(2,3-Dichlorophenyl)octahydropyridido[1,2-*a*]pyrazine-7-yl]acetoneitrile (53)

[(7*S*,9*aS*)-2-(2,3-Dichlorophenyl)octahydropyridido[1,2-*a*]pyrazine-7-yl] methyl-sulfonate (0.10 g, 0.26 mmol) was dissolved in dry DMSO (3 mL) and toluene (5 mL). The mixture was added to tetrabutylammonium cyanide (0.69 g, 2.55 mmol) and heated at 80 °C for 8 h. Then, the reaction mixture was cooled to room temperature and aqueous saturated NaHCO₃ was added. After extraction with ethyl acetate, the combined organic layers were dried (MgSO₄) and evaporated to give [(7*S*,9*aS*)-2-(2,3-dichlorophenyl)octahydropyridido[1,2-*a*]pyrazine-7-yl]acetoneitrile (64.0 mg, 77%) as a white solid. Mp 146–148 °C. ¹H NMR (CDCl₃, 360 MHz): δ 1.36 (dddd, $J = 4.0$ Hz, 11.0 Hz, 13.5 Hz, 14.0 Hz, 1H), 1.49 (dddd, $J = 2.5$ Hz, 2.5 Hz, 4.7 Hz, 13.5 Hz, 1H), 1.74 (dddd, $J = 4.5$ Hz, 4.5 Hz, 13.5 Hz, 13.5 Hz, 1H), 1.84 (dddd, $J = 2.5$ Hz, 2.5 Hz, 4.5 Hz, 13.5 Hz, 1H), 2.21–2.30 (m, 2H), 2.41 (dd, $J = 3.1$ Hz, 11.9 Hz, 1H), 2.49 (dd, $J = 10.2$ Hz, 10.9 Hz, 1H), 2.52 (ddd, $J = 3.0$ Hz, 11.2 Hz, 11.2 Hz, 1H), 2.67 (dd, $J = 7.7$ Hz, 16.8 Hz, 1H), 2.74–2.81 (m, 4H), 2.91 (ddd, $J = 2.7$ Hz, 11.3 Hz, 11.3 Hz, 1H), 3.21 (ddd, $J = 2.6$ Hz, 2.6 Hz, 10.9 Hz, 1H), 3.29 (ddd, $J = 2.7$ Hz, 5.2 Hz, 11.3 Hz, 1H), 6.97 (dd, $J = 3.0$ Hz, 6.6 Hz, 1H), 7.14–7.19 (m, 2H). ¹³C NMR (CDCl₃, 90 MHz): δ 19.6, 24.1, 26.9, 31.4, 51.3, 54.8, 57.1, 57.8, 61.1, 118.5, 119.8, 124.6, 127.4, 127.5, 134.1, 151.0. IR (NaCl): 3419, 2931, 2818, 2242 cm⁻¹. EI-MS m/z : 323, 325 (M⁺). Anal. (C₁₆H₁₉Cl₂N₃ · 0.25H₂O) C, H, N.

5.8. [(7*S*,9*aS*)-2-(2,3-Dichlorophenyl)octahydropyridido[1,2-*a*]pyrazine-7-yl]ethylamine (54)

A solution of [(7*S*,9*aS*)-2-(2,3-Dichlorophenyl)octahydropyridido[1,2-*a*]pyrazine-7-yl]acetoneitrile (45.0 mg, 0.14 mmol) in dry Et₂O (5 mL) was cooled to 0 °C and a solution of LiAlH₄ (1 M in Et₂O, 0.28 mL, 0.28 mmol) was added slowly. The mixture was allowed to warm up to room temperature and stirred for 1 h. Afterwards it was cooled again to 0 °C and quenched by cautious dropwise addition of water. The mixture was then filtered, and the filter cake was washed with diethyl ether (50 mL). The combined organic layers were washed with saturated NaHCO₃ and evaporated to give [(7*S*,9*aS*)-2-(2,3-dichlorophenyl)octahydro-pyridido[1,2-*a*]pyrazine-7-yl]ethylamine as a yellow oil (30.0 mg, 66%). ¹H NMR

(CDCl₃, 360 MHz): δ 1.33–1.46 (m, 2H), 1.55–1.68 (m, 3H), 1.78–1.84 (m, 2H), 2.14–2.18 (m, 1H), 2.27 (dd, $J = 3.0$ Hz, 11.3 Hz, 1H), 2.43 (ddd, $J = 2.7$ Hz, 11.4 Hz, 11.4 Hz), 2.50 (dd, $J = 10.4$ Hz, 10.4 Hz, 1H), 2.67–2.76 (m, 4H), 2.91 (ddd, $J = 2.7$ Hz, 11.4 Hz, 11.4 Hz), 3.14 (ddd, $J = 2.5$ Hz, 2.5 Hz, 10.4 Hz, 1H), 3.25 (ddd, $J = 2.7$ Hz, 5.0 Hz, 11.4 Hz, 1H), 6.67–6.71 (m, 1H), 6.73–6.80 (m, 1H), 6.92–6.99 (m, 1H, Phenyl). ¹³C NMR (CDCl₃, 90 MHz): δ 25.0, 27.8, 31.2, 35.4, 40.7, 51.3, 55.3, 57.1, 59.2, 61.6, 118.5, 124.4, 127.4, 127.5, 133.9, 151.3. IR (NaCl): 3361, 2928, 2854, 2817 cm⁻¹. EI-MS m/z : 327, 329 (M⁺). Anal. (C₁₆H₂₃Cl₂N₃) C, H, N.

5.9. Benzo[*b*]thiophene-2-carboxylic acid [(7*S*,9*aS*)-2-(2,3-dichlorophenyl)octahydro-pyridido[1,2-*a*]pyrazine-7-yl]ethyl amide (47)

To a solution of benzo[*b*]thiophene-2-carboxylic acid (purchased from *Acros Organics, Belgium*) (17.8 mg, 0.10 mmol), and DIPEA (0.07 mL, 0.42 mmol) in CH₂Cl₂ (3 mL) was added TBTU (42.0 mg, 0.13 mmol) in DMF (0.3 mL) at 0 °C. After addition of [(7*S*,9*aS*)-2-(2,3-dichlorophenyl)octahydropyridido[1,2-*a*]pyrazine-7-yl]ethylamine (40.0 mg, 0.13 mmol) in CH₂Cl₂ (5 mL), the mixture was stirred at room temperature for 1 h. Then, CH₂Cl₂ and aqueous saturated NaHCO₃ were added. The organic layer was dried (MgSO₄) and evaporated, and the residue was purified by flash chromatography (CH₂Cl₂–MeOH 98:2) to give benzo[*b*]thiophene-2-carboxylic acid [(7*S*,9*aS*)-2-(2,3-dichlorophenyl)octahydropyridido-[1,2-*a*]pyrazine-7-yl]ethyl amide as a white solid (35.0 mg, 71%). Mp 74–76 °C. ¹H NMR (CDCl₃, 360 MHz): δ 1.42–1.57 (m, 2H), 1.62–1.71 (m, 2H), 1.84–1.94 (m, 2H), 2.00–2.18 (m, 1H), 2.25 (dddd, $J = 3.0$ Hz, 3.0 Hz, 10.2 Hz, 10.2 Hz, 1H), 2.34 (dd, $J = 3.0$ Hz, 11.7 Hz, 1H), 2.47 (ddd, $J = 3.0$ Hz, 11.3 Hz, 11.3 Hz, 1H), 2.55 (dd, $J = 10.2$ Hz, 10.8 Hz, 1H, H-1_a), 2.74 (ddd, $J = 2.3$ Hz, 2.3 Hz, 11.3 Hz, 1H, H-4_e), 2.77 (d, $J = 11.7$ Hz, H-6_e), 2.89 (ddd, $J = 2.2$ Hz, 2.2 Hz, $J = 11.5$ Hz), 3.17 (ddd, $J = 2.5$ Hz, 2.5 Hz, 10.8 Hz, 1H, H-1_e), 3.22 (dd, $J = 2.2$ Hz, 11.5 Hz, 1H), 3.48 (ddd, $J = 6.3$ Hz, 6.5 Hz, 13.0 Hz, 1H), 3.59 (ddd, $J = 6.3$ Hz, $J = 13.0$ Hz, 13.0 Hz, 1H), 6.51 (br s, 1H), 6.88 (m, 1H, Phenyl), 7.13–7.16 (m, 2H, Phenyl), 7.39 (ddd, $J = 1.5$ Hz, 7.4 Hz, 7.4 Hz, 1H), 7.42 (ddd, $J = 1.5$ Hz, 7.4 Hz, 7.4 Hz, 1H), 7.75 (s, 1H), 7.81–7.86 (m, 2H). ¹³C NMR (CDCl₃, 90 MHz): δ 24.9, 27.8, 30.9, 31.6, 38.9, 51.2, 55.2, 57.1, 58.6, 61.8, 118.5, 122.7, 124.5, 124.9, 125.0, 126.2, 127.4, 127.5, 130.6, 134.0, 138.7, 139.1, 140.7, 151.1, 162.3. IR (NaCl): 3358, 3064, 2926, 2853, 1627 cm⁻¹. EI-MS m/z : 487, 489 (M⁺). Anal. (C₂₅H₂₇Cl₂N₃OS) C, H, N.

5.10. Receptor binding experiments

Receptor binding studies were carried out as described in the literature.^{46,47} In brief, the dopamine D1 receptor assay was done with porcine striatal membranes at a final protein concentration of 40 µg/assay tube and the radioligand [³H]SCH 23390 at 0.3 nM ($K_D = 0.95$ nM). Competition experiments with the human D2_{long},

D2_{short}, D3, and D4.4 receptors were run with preparations of membranes from CHO cells expressing the corresponding receptor and [³H]spiperone at a final concentration of 0.1 nM. The assays were carried out with a protein concentration of 3–10 µg/assay tube and K_d values of 0.06–0.14 nM for D2_{long}, 0.10–0.15 nM for D2_{short}, 0.22–0.35 nM for D3, and 0.28–0.33 nM for D4.4.

The investigation of serotonin 5-HT_{1A} and 5-HT₂ and adrenergic α_1 binding was performed as described in the literature.⁴⁸ In brief, porcine cortical membranes were subjected to the binding assay at a concentration of 80 µg/assay tube for determination of 5-HT_{1A} and 5-HT₂ binding utilizing [³H]8-OH-DPAT and [³H]ketanserin each at a final concentration of 0.5 nM with K_D values of 2.6 nM (for 5-HT_{1A}) and 1.9 nM (for 5-HT₂). Cortical membranes at 55 µg/assay tube and the radioligand [³H]prazosin at a final concentration of 0.4 nM were applied to determine adrenergic α_1 binding with K_D values of 0.08–0.10 nM.

Protein concentration was established by the method of Lowry using bovine serum albumin as standard.⁴⁹

Data analysis of the resulting competition curves was accomplished by non-linear regression analysis using the algorithms in PRISM (GraphPad Software, San Diego, CA). K_i values were derived from the corresponding EC₅₀ data utilizing the equation of Cheng and Prusoff.⁵⁰

Acknowledgments

The authors wish to thank Dr. H. H. M. Van Tol (Clarke Institute of Psychiatry, Toronto), Dr. J.-C. Schwartz and Dr. P. Sokoloff (INSERM, Paris) as well as J. Shine (The Garvan Institute of Medical Research, Sydney) for providing dopamine D₄, D₃, and D₂ receptor expressing cell lines, respectively, and Dr. R. Huff (Pfizer, Kalamazoo, MI) for providing dopamine D4.2 receptor expressing cells. This work was supported by the BMBF and Fonds der Chemischen Industrie.

References and notes

- Sokoloff, P.; Giros, B.; Martres, M. P.; Bouthenet, M. L.; Schwartz, J. C. *Nature* **1990**, *347*, 146.
- Richtand, N. M.; Woods, S. C.; Berger, S. P.; Strakowski, S. M. *Neurosci. Biobehav. Rev.* **2001**, *25*, 427.
- Joyce, J. N.; Millan, M. J. *Drug Discov. Today* **2005**, *10*, 917.
- Joyce, J. N.; Ryoo, H. L.; Beach, T. B.; Caviness, J. N.; Stacy, M.; Gurevich, E. V.; Reiser, M.; Adler, C. H. *Brain Res.* **2002**, *955*, 138.
- Bezard, E.; Ferry, S.; Mach, U.; Stark, H.; Leriche, L.; Boraud, T.; Gross, C.; Sokoloff, P. *Nat. Med.* **2003**, *9*, 762.
- Pilla, M.; Perachon, S.; Sautel, F.; Garrido, F.; Mann, A.; Wermuth, C. G.; Schwartz, J. C.; Everitt, B. J.; Sokoloff, P. *Nature* **1999**, *400*, 371.
- Unis, A. S.; Roberson, M. D.; Hill, K.; Hamblin, M. W.; Dorsa, D. W. In: 25th Annual Meeting of the Society of Neuroscience, San Diego, CA, Nov 11–16, 1995; Society of Neuroscience: Washington, DC, 1995.
- Boeckler, F.; Gmeiner, P. *Pharmacol. Ther.* **2006**, in press.
- Löber, S.; Hübner, H.; Utz, W.; Gmeiner, P. *J. Med. Chem.* **2001**, *44*, 2691.
- Löber, S.; Aboul-Fadl, T.; Hübner, H.; Gmeiner, P. *Bioorg. Med. Chem. Lett.* **2002**, *12*, 633.
- Löber, S.; Hübner, H.; Gmeiner, P. *Bioorg. Med. Chem. Lett.* **1999**, *9*, 97.
- Ortner, B.; Waibel, R.; Gmeiner, P. *Angew. Chem., Int. Ed.* **2001**, *40*, 1283.
- Newman, A. H.; Grundt, P.; Nader, M. A. *J. Med. Chem.* **2005**, *48*, 3663.
- Aston-Jones, G.; Druhan, J. *Nature* **1999**, *400*, 317.
- Boeckler, F.; Leng, A.; Mura, A.; Bettinetti, L.; Feldon, J.; Gmeiner, P.; Ferger, B. *Biochem. Pharmacol.* **2003**, *66*, 1025.
- Bettinetti, L.; Schlotter, K.; Hübner, H.; Gmeiner, P. *J. Med. Chem.* **2002**, *45*, 4594.
- Bettinetti, L.; Löber, S.; Hübner, H.; Gmeiner, P. *J. Comb. Chem.* **2005**, *7*, 309.
- Gmeiner, P.; Huebner, H.; Schlotter, K. WO2004004729, 2004.
- Lanig, H.; Utz, W.; Gmeiner, P. *J. Med. Chem.* **2001**, *44*, 1151.
- Boeckler, F.; Ohnmacht, U.; Lehmann, T.; Utz, W.; Hübner, H.; Gmeiner, P. *J. Med. Chem.* **2005**, *48*, 2493.
- Cha, M. Y.; Lee, I. Y.; Cha, J. H.; Choi, K. I.; Cho, Y. S.; Koh, H. Y.; Pae, A. N. *Bioorg. Med. Chem.* **2003**, *11*, 1293.
- Hackling, A.; Ghosh, R.; Perachon, S.; Mann, A.; Holtje, H. D.; Wermuth, C. G.; Schwartz, J. C.; Sippl, W.; Sokoloff, P.; Stark, H. *J. Med. Chem.* **2003**, *46*, 3883.
- Sybyl 6.9*, Tripos Inc., 1699 South Hanley Road, St. Louis, Missouri, 63144, U.S.A.
- Clark, M.; Cramer, R. D., III; Van Opdenbosch, N. *J. Comput. Chem.* **1989**, *10*, 982.
- Gasteiger, J.; Marsili, M. *Tetrahedron* **1980**, *36*, 3219.
- Hinze, J.; Jaffe, H. H. *J. Am. Chem. Soc.* **1962**, *84*, 540.
- Stewart, J. J. *J. Comput. Aided Mol. Des.* **1990**, *4*, 1.
- Stewart, J. J. P.; Frank, J. *MOPAC*, Seiler Bokstav Research Laboratory, United Air Force Academy, CO 80840.
- ASP V3.22*, Oxford Molecular Ltd, The Medawar Centre, Oxford Science Park, Sandford-on-Thames, Oxford OX4 4GA, U.K.
- TSAR V3.2*, Oxford Molecular Ltd, The Medawar Centre, Oxford Science Park, Sandford-on-Thames, Oxford OX4 4GA, U.K.
- Beck, B.; Clark, T.; Glen, R. C. *J. Mol. Model.* **1995**, *1*, 176.
- Clark, T.; Alex, A.; Beck, B.; Chandrasekar, J.; Gedeck, P.; Horn, A.; Huttern, M.; Martin, B.; Rauhut, G.; Sauer, W.; Schindler, T.; Steinke, T. *VAMP 7.0 Program Package*; Oxford Molecular Plc: Oxford, 1998.
- Tropsha, A.; Cho, S. J. In *3D QSAR in Drug Design*; Kubinyi, H., Ed.; ESCOM: Leiden, 1998; Vol. 3, pp 57–69.
- Wang, R.; Gao, Y.; Liu, L.; Lai, L. *J. Mol. Model.* **1998**, *4*, 276.
- Wold, S. *Quant. Struct.-Act. Relat.* **1991**, *10*, 191.
- Cramer, R. D., III; Patterson, D. E.; Bunce, J. D. *J. Am. Chem. Soc.* **1988**, *110*, 5959.
- Shao, J. *J. Am. State Assoc.* **1993**, *88*, 486.
- Baroni, M.; Clementi, S.; Cruciani, G.; Costantino, G.; Riganelli, D.; Oberrauch, E. *J. Chemom.* **1992**, *6*, 347.
- Cruciani, G.; Baroni, M.; Clementi, S.; Costantino, G.; Riganelli, D.; Skagerberg, B. *J. Chemom.* **1992**, *6*, 335.

40. Böhm, M.; Stürzebecher, J.; Klebe, G. *J. Med. Chem.* **1999**, *42*, 458.
41. Thibaut, U.; Folkers, G.; Klebe, G.; Kubinyi, H.; Merz, A.; Rognan, D. In *3D QSAR in Drug Design. Theory, Methods and Applications*; Kubinyi, H., Ed.; ESCOM: Leiden, The Netherlands, 1993; pp 711–716.
42. Hattotuwigama, C. K.; Doytchinova, I. A.; Flower, D. R. *J. Chem. Inf. Mod.* **2005**, *45*, 1415.
43. Bright, G. M.; Desai, K. A. WO9008148, 1990.
44. Hartwig, J. F. *Angew. Chem., Int. Ed.* **1998**, *37*, 2046.
45. Wolfe, J. P.; Tomori, H.; Sadighi, J. P.; Yin, J.; Buchwald, S. L. *J. Org. Chem.* **2000**, *65*, 1158.
46. Hübner, H.; Haubmann, C.; Utz, W.; Gmeiner, P. *J. Med. Chem.* **2000**, *43*, 756.
47. Lenz, C.; Haubmann, C.; Hübner, H.; Boeckler, F.; Gmeiner, P. *Bioorg. Med. Chem.* **2005**, *13*, 185.
48. Schlotter, K.; Boeckler, F.; Hübner, H.; Gmeiner, P. *J. Med. Chem.* **2005**, *48*, 3696.
49. Lowry, O. H.; Rosebrough, N. J.; Farr, A. L.; Randall, R. *J. J. Biol. Chem.* **1951**, *193*, 265.
50. Cheng, Y.; Prusoff, W. H. *Biochem. Pharmacol.* **1973**, *22*, 3099.
51. Clark, R. D.; Sprous, D. G.; Leonard, J. M. In *Rational Approaches to Drug Design*; Hoeltje, H.-D., Sippl, W., Eds.; Prous Science SA: 2001; pp 475–485.